

# Study on Classification of Metal Objects by Fluxgate Magnetometer Cube Structure

songtong han (✉ [hansongtong@njust.edu.cn](mailto:hansongtong@njust.edu.cn))

Nanjing University of Science and Technology

Bo Zhang

the army engineering university of PLA <https://orcid.org/0000-0002-7720-9801>

zhu wen

Sichuan Police College

---

## Research Article

**Keywords:** Magnetic targets, ResNet-18, Classification, Magnetic dipole

**Posted Date:** April 19th, 2022

**DOI:** <https://doi.org/10.21203/rs.3.rs-1532750/v1>

**License:** © ⓘ This work is licensed under a Creative Commons Attribution 4.0 International License.

[Read Full License](#)

---

# Abstract

In order to classification the kinds of metal objects, we propose a recognition method based on ResNet-18. First, we built a magnetic field feature collector that we called FMCAS (Fluxgate magnetometer cube arrangement structure), using 8 fluxgate magnetometer sensor array structures to ensure a distance of 400mm between each sensitive unit. We use FMCAS to collect the magnetic field data of a survey line along the east-west direction on the north side of the measured target. Next, we change the location and type of the target and build a database of magnetic target models, which enriches the diversity of the training dataset. Construct the magnetic flux density tensor matrix to create the experimental dataset. Finally, we use the improved ResNet-18 to train the data to get the recognition classification recognizer. The recognition accuracy of this approach is 84.1%, according to the test results from 107 groups of validation sets. The target with larger magnetic moment has the best recognition effect, with a recognition accuracy rate of 96.3%, a recall rate of 96.4%, and a precision rate of 96.4%. Experimental results show that our improved ResNet-18 network can effectively handle the classification of metal objects.

## 1. Introduction

In our living environment, we are surrounded by the geomagnetic field. When a metal target (mainly including iron, cobalt, nickel, etc.) is infiltrated into the geomagnetic field, the target will be magnetized by the geomagnetic field, and a secondary field will be generated in the original magnetic field space, which will distort the surrounding magnetic field [1]. By measuring the magnetic field in space to determine the underground [2] [3] or underwater metal targets [4], it has a wide range of applications in the field of finding mines [5].

There are many technical means for metal target detection, and magnetic detection is one of the commonly used technical means. Total magnetic field detection, vector magnetic field detection, gradient magnetic field detection, and gradient tensor magnetic field detection are all common methods of space magnetic field measurement [5]. Different methods of measuring the space magnetic field lead to different numbers of sensors, and sensors with reasonable arrangement will obtain more space magnetic field information [6]. Therefore, in recent years, many scholars [7] [8] have adopted the technical means of multi-sensor cooperation in the process of metal target detection and localization research.

There are various external shapes of metal targets. If the target is far away from the observation point, the target can be approximately regarded as a magnetic dipole model [9]. Jin Huanghuang scholar [10] proposed to use the equivalent method of the simplest dipole model to replace the target, which can greatly simplify the identification and inversion of metal targets. Stephen [11] regarded the metal target as a magnetic dipole, and identified the detection target by analyzing the magnitude and direction of the dipole. Bülent [12] regarded the metal target as a dipole, and performed tensor analysis to locate the metal target using tensor invariants. These scholars can identify the location of metal targets through different

algorithms in the study of metal target location and identification, but it is difficult to identify the types of metal targets due to the limitations of their own algorithms.

The metal object recognition problem is a highly nonlinear problem. Billings [13] proposed that the type of metal target can be inferred by obtaining the angle between the remanent magnetization of the metal target and the geomagnetism. This method has high efficiency but imperfect resolution. Beran [14] derives the metal target by solving the objective function. In the process of solving the loss function, since the forward model is nonlinear, the result will fall into a local minimum. Mark [15] suggested a method for inferring metal targets using magnetic data in a probabilistic manner. Various iterative processes are used, or the multi-chain Markov Chain Monte Carlo (McMC) approach is used. The approach is unaffected by the inversion process's start point, allowing it to avoid numerous local minima in the highly nonlinear model space and iteration. However, this strategy does not eliminate the need to choose a starting value. It will be much more harder to repeat subsequently when there's no preceding condition.

In the field of metal target recognition, Zhou[16] suggested a shallow magnetic tiny target detection and classification approach based on RCNN. In the research process, the  $G_{zz}$  element of the magnetic gradient tensor has been chosen as the data source. To identify the target, create a Mask-RCNN algorithm. L-shaped, concave, spherical, and cuboid detection targets are utilized in the study procedure, and variations in the environmental magnetic field are not incorporated in the classification process, therefore the research findings are still theoretical. Furthermore, because Zhou only employed the  $G_{zz}$  component to extract characteristics in his research, the magnetic features of the target are insufficient.

On the basis of the foregoing, this research offers a methodology based upon that ResNet-18 deep learning model for identifying the sorts of metal items. Using the magnetic field data of a survey line, extract the 8 fluxgate magnetometer data on the north side of the target and precisely identify the type of subsurface metal targets.

## 2. Methods

### A. space magnetic flux density acquisition

When the metal target is far away from the observation point, we can approximately think that the magnetization field model of the metal target is equivalent to the magnetic dipole model [17]. The magnetic field distribution of the magnetic dipole in space can be expressed by the following formula [18].

$$B_{dipolar}(r) = \frac{\mu_0}{4\pi} \frac{1}{r^3} [3(m \cdot \hat{r})\hat{r} - m]$$

(1)

Among them,  $m$  is the dimension of the magnetic moment [ $L^2I$ ];  $r$  denotes the distance between the magnetic dipole's center and the observation point;  $\hat{r}$  denotes the unit vector between the magnetic dipole's center and the observation point; and  $\mu_0$  denotes the vacuum permeability.

In order to obtain more data of spatial magnetic anomalies and ensure that the distance between each fluxgate sensitive unit is 400mm, we adopted an array structure arrangement of 8 three-axis fluxgate magnetometers (model HSF923-2H5-AA Xi'an Huashun). We call this structure Fluxgate magnetometer cube arrangement structure (FMCAS), as shown in Fig. 1. Each fluxgate magnetometer obtains  $xyz$  three-axis magnetic flux data, so FMCAS obtains 8  $xyz$  three-axis magnetic flux data, a total of 24 groups of data.

We acquire an east-west magnetic field data measurement line north of the detection target. As shown in Fig. 2., We connect the FMCAS to the Sliding Block through copper bolts and place it on the Sliding Track made of aluminum alloy. The laser distance sensor (model L-GAGE) records the distance information of the position of the FMCAS relative to the sensor. The material of the sliding block is wood, in order to facilitate sliding, we smeared grease on the sliding track. Each time the assistant pulls the sliding track with the rope, we obtain experimental data on a measuring line.

Through the above experimental method, we can get the magnetic field data of a survey line every time we slide the sliding block, which contains the target magnetic anomaly. We intercept the middle part of the survey line (the data at both ends fluctuates greatly when sliding starts and ends), divide the intercepted part of the survey line into 100 equal parts, and obtain 101 position coordinates. Corresponding the FMCAS magnetic flux density data of each position to obtain a set of  $101 \times 24$  size magnetic flux data about the position information.

We might as well define the pseudo-total field  $xyz_i$  of the fluxgate magnetometer (because the fluxgate magnetometer has not been calibrated) as follows:

$$xyz_i = \sqrt{x_i^2 + y_i^2 + z_i^2} (i = 1, 2, \dots, 8)$$

The pseudo-total field of the  $i$ th fluxgate magnetometer is represented by  $xyz$  in the formula. The  $i$ th fluxgate magnetometer's x-axis magnetic field output is  $x_i$ ; the  $i$ th fluxgate magnetometer's y-axis magnetic field output is  $y_i$ ; and the  $i$ th fluxgate magnetometer's z-axis magnetic field output is  $z_i$ .

We construct the magnetic flux tensor matrix as shown in Fig. 3, the matrix size is  $[101, 8, 4]$ . The first dimension includes 101 position information; the second dimension includes the label information of 8 fluxgate magnetometers; the third dimension includes the  $xyz$  pseudo total field, the x-axis magnetic field, the y-axis magnetic field, and the component information of the z-axis magnetic field.

Later, we will use the above-mentioned magnetic flux tensor matrix to train the recognition algorithm.

## B. ResNet-18

Four Chinese, including Microsoft Research Institute's Kaiming He, proposed ResNet (Residual Neural Network). With an error rate of 3.57% on top5, a 152-layer neural network was successfully trained and won the championship in the ILSVRC2015 competition utilizing ResNet Unit. ResNet's topology allows for rapid neural network training while also considerably improving model accuracy.

When deepening the neural network, the problem of gradient explosion and disappearance occurs. And we also use normalized initialization [19–21] and intermediate normalization layers [22] to solve this problem. Due to the existence of the nonlinear activation function Relu, each input-to-output process is almost irreversible (information loss) [23]. It is difficult to reverse the full input from the output, which also makes it very unlikely that the features will be fully preserved as the forward propagation layer by layer. The Residual Learning module is introduced into the deep neural network, and the output before the previous layer (or layers) is added to the output calculated by this layer by jumping, and the summation result is input into the activation function as the function of this layer. output [24]. In this way, the depth of the network can be greatly increased. The main structure of ResNet is shown in Table 1.

Table 1  
ResNet architectures with different layers

layer name	output size	18-layer	50-layer
conv1	112×112	7×7, 64, stride 2	
conv2_x	56×56	3×3max pool, stride 2	
		$\begin{bmatrix} 3 \times 3, 64 \\ 3 \times 3, 64 \end{bmatrix} \times 2$	$\begin{bmatrix} 1 \times 1, 64 \\ 3 \times 3, 64 \\ 1 \times 1, 256 \end{bmatrix} \times 2$
conv3_x	28×28	$\begin{bmatrix} 3 \times 3, 128 \\ 3 \times 3, 128 \end{bmatrix} \times 2$	$\begin{bmatrix} 1 \times 1, 128 \\ 3 \times 3, 128 \\ 1 \times 1, 512 \end{bmatrix} \times 4$
conv4_x	14×14	$\begin{bmatrix} 3 \times 3, 256 \\ 3 \times 3, 256 \end{bmatrix} \times 2$	$\begin{bmatrix} 1 \times 1, 256 \\ 3 \times 3, 256 \\ 1 \times 1, 1024 \end{bmatrix} \times 6$
conv5_x	7×7	$\begin{bmatrix} 3 \times 3, 512 \\ 3 \times 3, 512 \end{bmatrix} \times 2$	$\begin{bmatrix} 1 \times 1, 512 \\ 3 \times 3, 512 \\ 1 \times 1, 2048 \end{bmatrix} \times 3$
1×1		average pool, 1000-d fc, softmax	

We are conducting research on object classification and recognition, utilizing the main network architecture of ResNet-18. In practice, we make the following modifications to the original ResNet-18:

Step 1. Removed the first layer of  $7 \times 7$  convolution in the original network;

Step 2. Modify the original second layer  $3 \times 3$  maximum pooling layer to  $3 \times 3$  convolution, and set 64 convolution kernels.

Step 3. Finally, modify the 1000 neurons in the final fully connected layer to 3 neurons.

Through the above processing we get an improved ResNet-18 network. The magnetic feature data is in the data format of  $101 \times 8 \times 4$ , and the convolution operation is performed through a  $3 \times 3$  convolution kernel, and then it is input into 8 ResNet blocks in turn, and the corresponding convolution operation is performed. The data is then globally pooled before being fed into the fully connected layer. Figure 4 depicts the network structure. The data is then globally pooled before being fed into the fully connected layer. Figure 4 depicts the network structure.

## 2. training ResNet-18 model

On an NVIDIA GeForce RTX 2080 Ti GPU with 32 GB of memory, all model training and test evaluation experiments were carried out. The TensorFlow GPU version operates on Windows 10 and is installed on the Anaconda 3 platform.

### A. Dataset generation

We used three various sizes of iron balls as neural network training and recognition targets in the experiment. The 5m-long sliding track is located on the north side of the detection target, and the laser distance sensor used to record the FMCAS position information is located on the east side of the sliding track. The data collector (model: PXIe-4309-NI) is located 4m northeast of the slide rail, as shown in Fig. 5.

A spatial Cartesian coordinate system is developed, as shown in Fig. 6, with the X axis facing north, the Y axis facing west, and the unit being meters. The start of the sliding track is at coordinates (0.5, -2), and the finish of the sliding track is at coordinates (0.5, -2). The FMSC slides from the sliding track start point to the sliding track end point. The sliding distance is 4 meters. During the sliding process, the laser distance sensor records the distance (0 ~ 4) of the FMSC relative to the starting point of the slide rail in real time.

The starting position of each probe target is (-0.2, -0.2) and the end position is (0.2, 0.2). The target moves 0.1 meters along the x-axis each time. When the x-axis coordinate of the target reaches 0.2 meters, the target moves 0.1 meters along the y-axis. Repeatedly adjust the x-axis position of the target to complete a cycle. The target has a total of 25 position points, and each position point FMCAS slides 40 times. Each target to be tested has a total of 1000 groups of data, which are used as the training set of deep learning. The targets are randomly arranged in 5 random positions within a square area from (-0.2, -0.2) to (0.2, 0.2), and the FMCAS is also slid 40 times, with a total of 200 groups of data for each target,

as the test set of deep learning. During the experiment, the three targets we measured and their effective data are shown in Table 2.

Table 2  
Statistical table of measured data

Detection Target	Properties (Radius/mm)	Valid data (Groups)	Invalid data (Groups)
No. 1 iron ball	51	1238	0
No. 2 iron ball	56.5	1223	0
No. 3 iron ball	67.5	1240	1

During the experiment, we set the sampling frequency to 100Hz. The space where the experiment is located is disturbed by the power frequency signal, and the magnetic anomaly caused by the target we are concerned about is the DC component. Therefore, in signal processing, we use the Butterworth filter to low-pass filter the collected time-domain signal. We set the bandpass frequency of the filter to be 2Hz, the bandstop frequency to be 12Hz, and the order of the filter to be 6th order. The comparison before and after low-pass filtering is shown in Fig. 7. The red curve represents the unfiltered time-domain signal, and the black line represents the low-pass filtered time-domain signal.

We choose the starting point of the magnetic tensor matrix at the position of 1000mm from the FMCAS to the laser distance sensor, and the end point at the position of 4000mm. We divide 101 points evenly within the distance of 3000mm, and obtain the three-axis magnetic flux density output of each fluxgate magnetic sensor at these distance points. We use the position of the FMCSA as the independent variable, and use the three-axis magnetic flux density of each fluxgate magnetic sensor as the dependent variable for interpolation calculation. We use the position of the FMCAS as the independent variable, and use the three-axis magnetic flux density of each fluxgate magnetic sensor as the dependent variable for interpolation calculation. Using the linear interpolation method of sample points, according to the position we need, the three-axis magnetic flux density distribution of each fluxgate magnetic sensor at this position. In this way, we can obtain the 3-axis magnetic field data of the 8-fluxgate sensor at 101 equally spaced positions between 1000mm and 4000mm. The interpolation process is shown in Fig. 8.

According to the above processing method, we process each set of data into a set of magnetic flux tensor matrices. and map the resulting matrix to the labels one-to-one.

## B. Training of recognition network

We separated the data set into 3088 training sets, 513 test sets, and 100 validation sets, according to Table 2. The three sets are mutually exclusive and completely separate from one another. After 100 iterations, the model took 4 hours to train, and the iteration curve is illustrated in Fig. 9.

For the sample set D, the classification accuracy is defined as the following formula.

$$\text{acc}(f; D) = \frac{1}{m} \sum_{i=1}^m \mathbb{I}(f(x_i) = y_i)$$

The  $f$  function represents the completely trained neural network, and  $m$  indicates the total number of all samples. The accuracy of the training set steadily increases as the number of iterations grows, eventually converges to 1; the accuracy of the test set gradually increases after the 60th iteration, eventually converges to roughly 0.9. We added 7 sets of untargeted ambient magnetic fields to the validation set, totaling 107 groups, to further verify the recognition effect. Table 3 shows the test labels in the final validation set.

Table 3  
Validation set contains label table

Detection Target	Valid data (Groups)
No. 1 iron ball	40
No. 2 iron ball	32
No. 3 iron ball	28
No see	7

For the problem of target recognition accuracy, we add an untargeted environmental magnetic field. We set the target recognition threshold to 0.75. During the recognition process, if it is inferred that the recognition target has a probability of more than 75% and is identified as a target in the target library, we consider this target recognition to be effective. If it is inferred that the recognition probability of the recognized target is 75%, then we think that the target we detected is not in the target library, and the detected target is No see. Bringing the validation set into the model resulted in an accuracy of 84.1%. The recall rate, accuracy rate, and F1 value are used as assessment indicators to assess the model's performance.

$$\text{Recall} = \frac{TP}{TP + FN}$$

$$\text{Precision} = \frac{TP}{TP + FP}$$

$$\text{Specificity} = \frac{TN}{TN + FP}$$

$$F_1 = \frac{2 \times \text{Recall} \times \text{Precision}}{\text{Recall} + \text{Precision}}$$

TP (True Positive) denotes a true case; FP (False Positive) denotes a false positive example; and FN (False Negative) denotes a false negative example. Figure 10 depicts the confusion matrix derived by calculation.

The model's accuracy rating is 84.1% after calculations. Table 4 shows the precision rate, recall rate, single accuracy rate, and F1 value.

Table 4  
Model reference index table

	Precision	Recall	Acc_single	F1
No. 1 iron ball	88.2%	75%	86.9%	0.81
No. 2 iron ball	87.5%	87.5%	92.5%	0.87
No. 3 iron ball	96.4%	96.4%	96.3%	0.96
No see	38.5%	71.4%	90.6%	0.5

### 3. Experimental Results And Analysis

By observing Fig. 9, it can be found that the accuracy of the validation set begins to converge after 60 iterations, and the accuracy of the validation set tends to fluctuate smoothly after 80 iterations, and finally converges to about 0.9.

Through the analysis of recall rate, accuracy rate and F1 value calculated by the model, it can be seen that in the process of target classification and recognition, the single recognition accuracy of No. 3 iron ball is the highest, and the F1 index is closest to 1. The identification between No. 1 iron ball and No see is relatively difficult because the local geomagnetic environment itself has magnetic anomalies, and the diameter of No. 3 iron ball is relatively small, which is not conducive to distinguishing the difference between the target and the environment. In other words, the magnetic anomaly caused by the No. 1 iron ball is sometimes overwhelmed by the local environment, so the recognition algorithm cannot accurately distinguish between the two. Similarly, the recognition algorithm will also confuse some No. 2 iron balls with No. 1 iron balls, because the magnetic anomalies between the two are not very different. In contrast, the algorithm is more accurate in distinguishing No. 1 iron balls and No. 3 iron balls.

This shows that the algorithm still has a certain ability to identify targets with large differences in magnetic anomalies.

### 4. Conclusion

When distinguishing metal targets through this recognition algorithm, the overall accuracy rate is 84.1%. The No. 3 iron ball performed the best in recognition, with a single recognition accuracy rate of 96.3%, a recall rate of 96.4%, and a precision rate of 96.4%. The excellent performance is attributed to the fact that the target itself is larger than other targets, and the magnetic anomaly is more obvious. When the algorithm recognizes the target with a relatively close volume, it will be accompanied by the generation of errors. In the experiment, the No. 1 iron ball and the No. 2 iron ball will be misclassified, because the

volumes of the two are relatively close and the magnetic anomalies displayed on the fluxgate magnetic field sensor are relatively close.

Overall, our improved RestNet-18 network can effectively handle the classification of metal objects.

## Declarations

### Acknowledgements

The authors would like to acknowledge the National Natural Science Foundation of china (Grant No. 61801511) , the Natural Science Foundation of Jiangsu Province (Grant No. BK20180580) and Postgraduate Research & Practice Innovation Program of Jiangsu Province (Gant No. KYCX20\_0311) to provide fund.

### Author contributions:

Songtong Han contributed to the conception of the study;

Bo Zhang performed the experiment;

Zhu Wen contributed significantly to analysis and manuscript preparation.

## References

1. BUSCHOW K H J, DE BOER F R (2003) Physics of Magnetism and Magnetic Materials [M]. Springer US
2. PANG H, LUO S, ZHANG Q et al (2013) Calibration of a fluxgate magnetometer array and its application in magnetic object localization [J]. Meas Sci Technol 24(7):075102
3. HAN S, RONG X, BIAN L, et al (2019) [C] The application of magnetometers and electromagnetic induction sensors in UXO detection; proceedings of the E3S Web of Conferences, F, EDP Sciences
4. SHAN S, ZHANG H, ZHOU S et al (2020) [C] On Real-time Tracking for Underwater Magnetic Target with Extension Considerations; proceedings of the 2020 7th International Forum on Electrical Engineering and Automation (IFEEA), F, IEEE
5. OBIORA D N, OHA I A, IHEDIKE A O et al (2021) Comparative depth estimates and modeling of magnetic anomalies over the Nkalagu area, Southeastern Nigeria [J]. Modeling Earth Systems and Environment, 1–19
6. LIU H, ZHAO C, WANG X et al (2021) A multi-magneto-inductive sensor array system for real-time magnetic field imaging of ferromagnetic targets [J]. Rev Sci Instrum 92(3):035113
7. LI Q, LI Z, ZHANG Y et al (2018) Integrated compensation and rotation alignment for three-axis magnetic sensors array [J]. IEEE Trans Magn 54(10):1–11

8. YIN G, LI P, WEI Z et al Magnetic dipole localization and magnetic moment estimation method based on normalized source strength [J]. *Journal of Magnetism and Magnetic Materials*, 502(
9. HAN S-T ZHANG B, RONG X-L et al (2021) A Calculation Method of Magnetic Anomaly Field Distribution of Ellipsoid with Arbitrary Posture [J]. *International Journal of Pattern Recognition and Artificial Intelligence*, 2154031
10. JIN, H-H, ZHUANG Z-H, FU M-Y et al (2021) Modeling method using simplest multiple magnetic dipoles equivalence [J]. *Syst Eng Electron Technol* 43(08):2066–2075
11. BILLINGS SD, PASION C (2006) Magnetic models of unexploded ordnance [J]. *IEEE Trans Geosci Remote Sensing* 44(8):2115–2124
12. ORU B. Location and depth estimation of point-dipole and line of dipoles using analytic signals of the magnetic gradient tensor and magnitude of vector components [J]. *Journal of Applied Geophysics*, 70(1):27–37
13. BILLINGS SD, PASION L R, OLDENBURG D W (2002) [C] Inversion of magnetics for UXO discrimination and identification; proceedings of the Proc 2002 UXO Forum, Orlando, FL, F, Citeseer
14. BERAN L, BILLINGS S (2011) Incorporating Uncertainty in Unexploded Ordnance Discrimination [J]. *IEEE Trans Geoscience Remote Sens* 49(8):3071–3080
15. WIGH M D, HANSEN T M, D SSING A (2019) Inference of unexploded ordnance (UXO) by probabilistic inversion of magnetic data [J]. *Geophys J Int* 220(1):37–58
16. ZHOU Z, ZHANG M, CHEN J et al (2020) Detection and Classification of Multi-Magnetic Targets Using Mask-RCNN [J]. *IEEE Access* 8:187202–187207
17. Irvine JM (1981) Introduction to Electrodynamics [J]. *Am J Phys* 32(10):331
18. WIEGERT R, LEE K (2008) OESCHGER J. Improved magnetic STAR methods for real-time, point-by-point localization of unexploded ordnance and buried mines; proceedings of the Oceans, F, [C]
19. GLOROT X, BENGIO Y Understanding the difficulty of training deep feedforward neural networks; proceedings of the Proceedings of the thirteenth international conference on artificial intelligence and statistics, F, 2010 [C]. *JMLR Workshop and Conference Proceedings*
20. HE K, ZHANG X, REN S, et al (2015) Delving Deep into Rectifiers: Surpassing Human-Level Performance on ImageNet Classification; proceedings of the CVPR, F, [C]
21. SAXE A M, MCCLELLAND J L, GANGULI S (2014) Exact solutions to the nonlinear dynamics of learning in deep linear neural networks [J]. *Computer Science*,
22. IOFFE S (2015) [C] SZEGEDY C. Batch normalization: Accelerating deep network training by reducing internal covariate shift; proceedings of the International conference on machine learning, F, PMLR
23. SANDLER M, HOWARD A, ZHU M et al (2018) Mobilenetv2: Inverted residuals and linear bottlenecks; proceedings of the Proceedings of the IEEE conference on computer vision and pattern recognition, F, [C]
24. HE K, ZHANG X, REN S, et al (2016) Deep residual learning for image recognition; proceedings of the Proceedings of the IEEE conference on computer vision and pattern recognition, F, [C]

# Figures

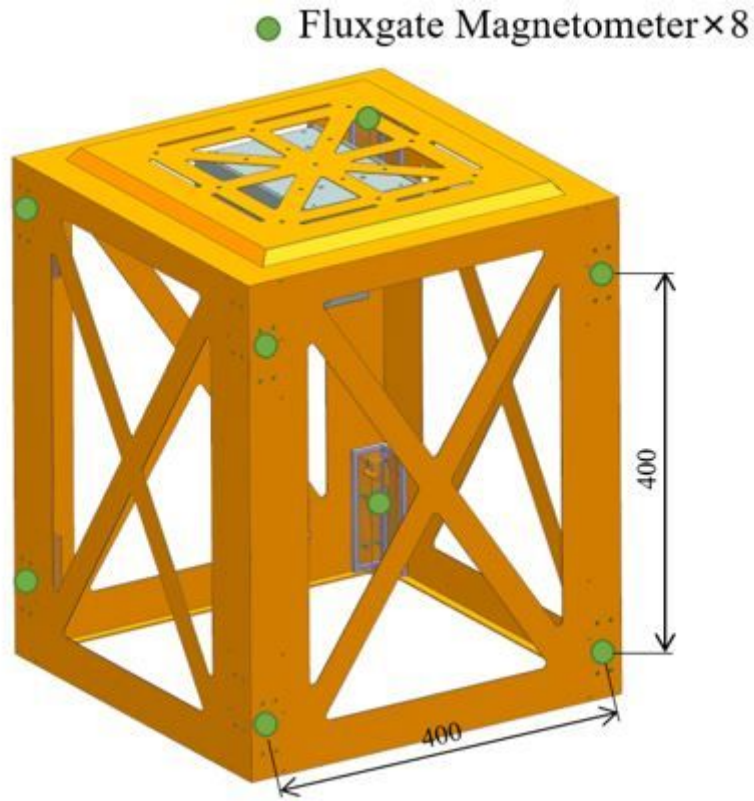


Figure 1

The diagram of FMCAS

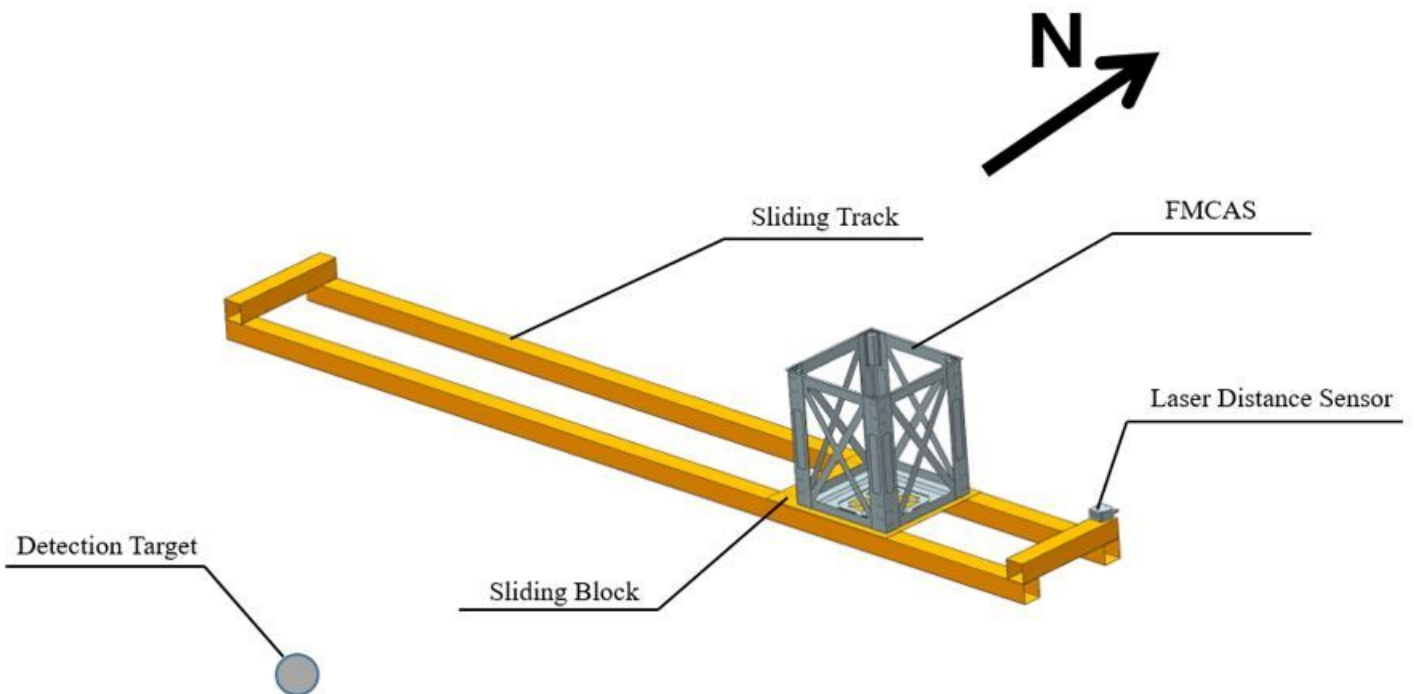
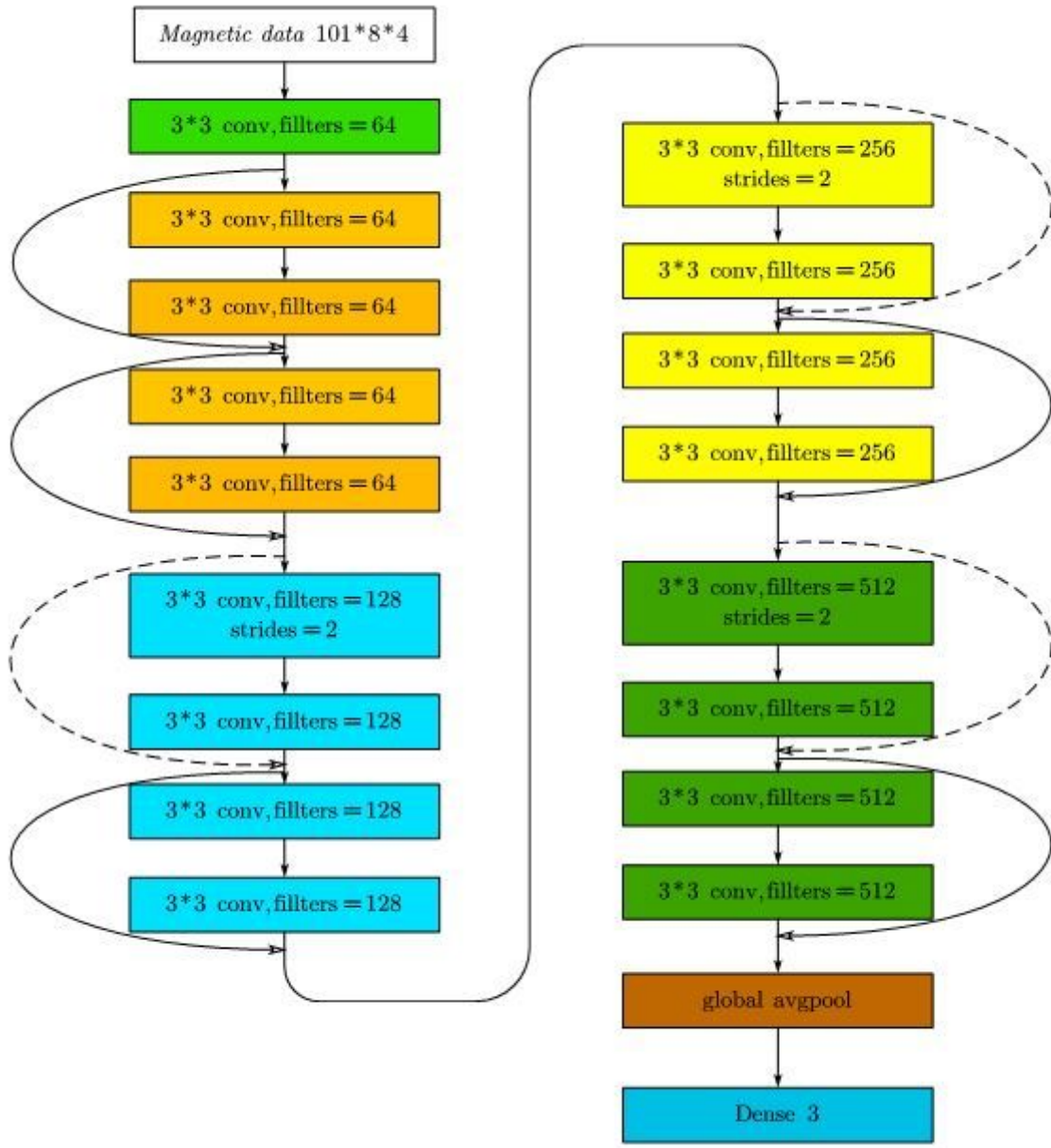


Figure 2





**Figure 4**

RstNet18 network structure. The dotted line indicates that the dimensions are different, and it needs to be adjusted through a 1x1 convolution kernel to adjust to the same dimension.

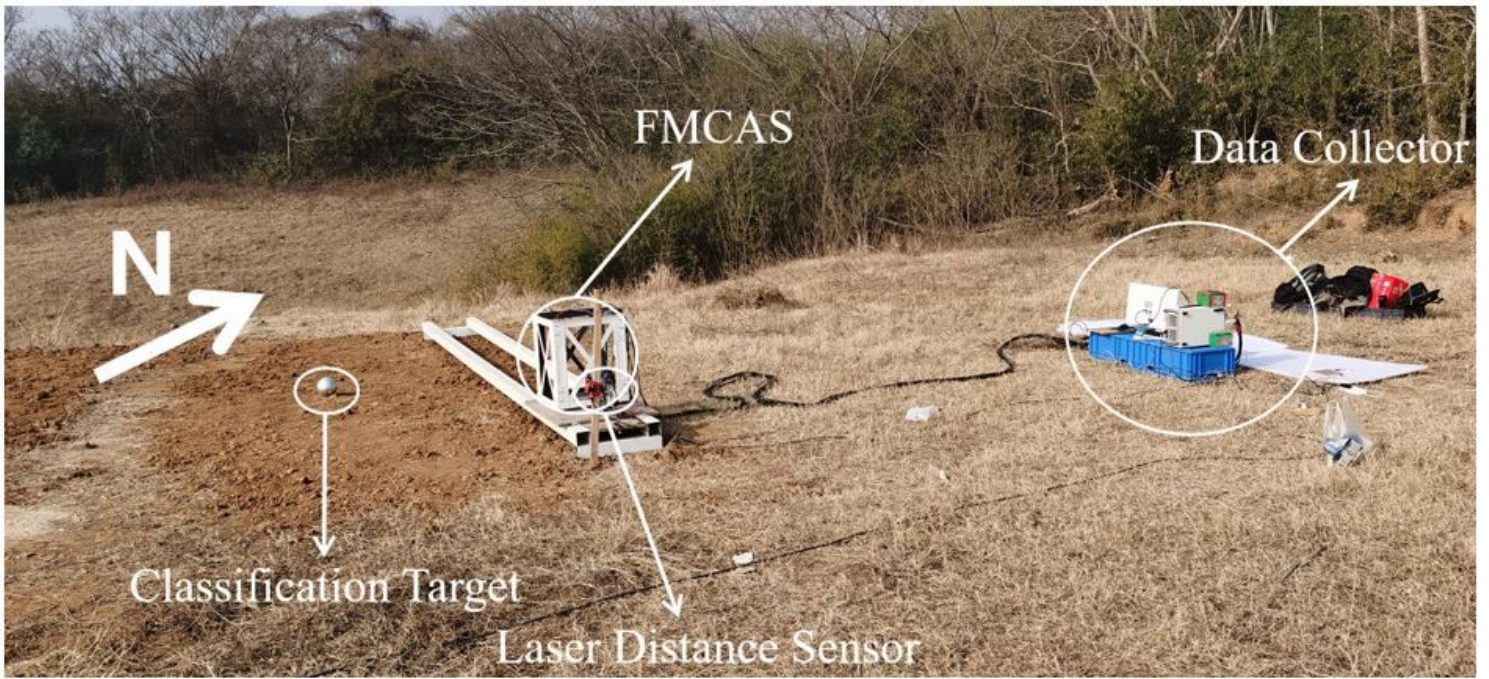
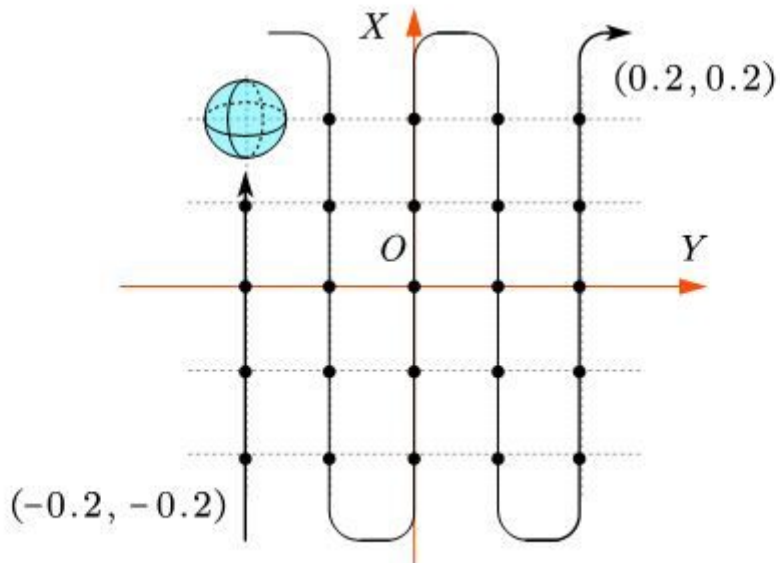
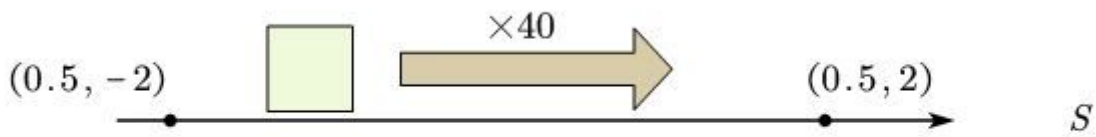


Figure 5

Photos of the experimental environment

*N*



**Figure 6**

Detection Plan

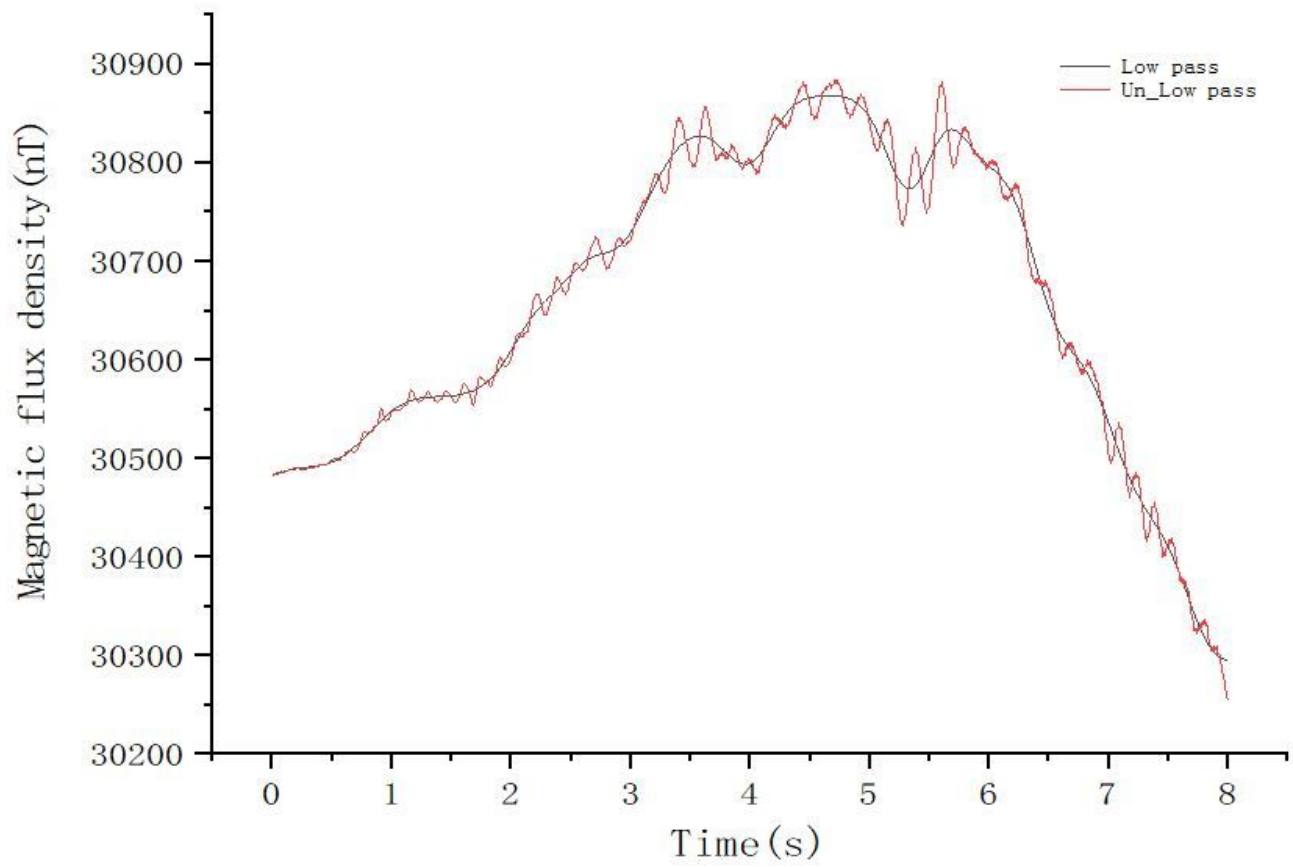


**Figure 7**

Comparison of time domain signals before and after filtering

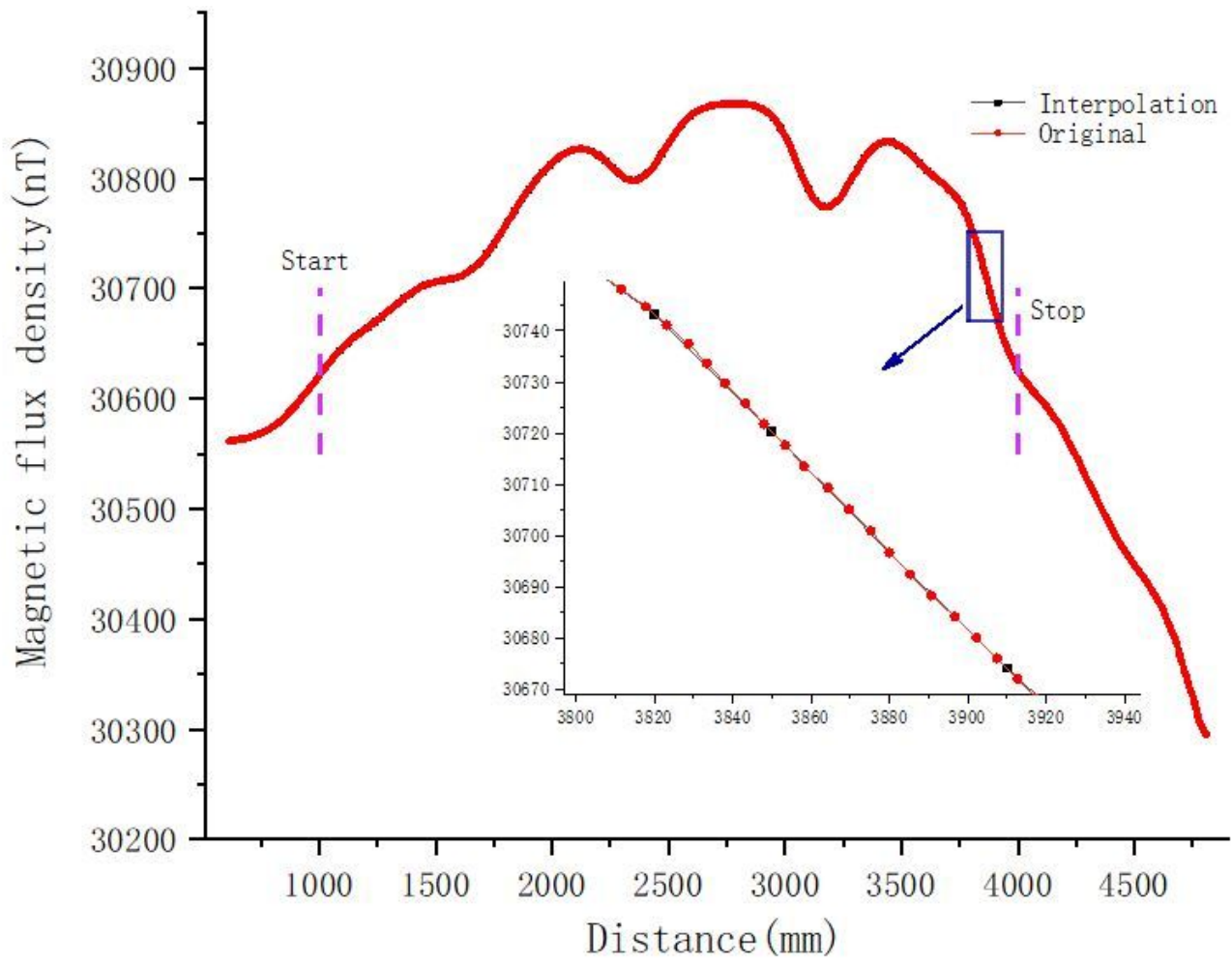


**Figure 8**

Interpolation calculation of magnetic field position distribution

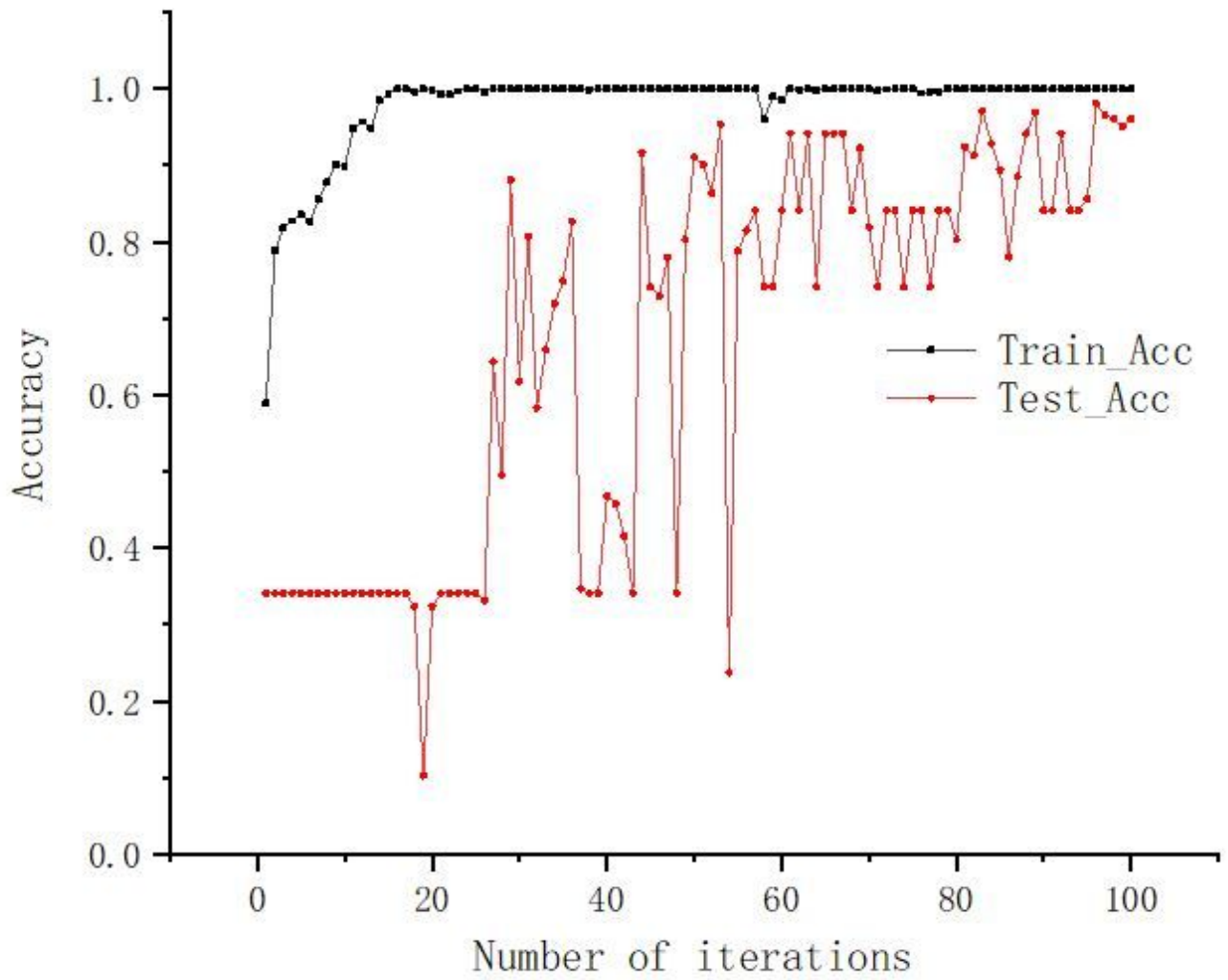


**Figure 9**

Curve of Iterative Convergence. The accuracy on the training set is shown by the black line, while the accuracy on the test set is represented by the red line.



Figure 10

Confusion Matrix